Mon. Not. R. Astron. Soc. **348,** 846–856 (2004) doi:10.1111/j.1365-2966.2004.07398.x

Radiatively driven electron–positron jets from two-component accretion flows

Indranil Chattopadhyay,[1⋆] Santabrata Das[2⋆] and Sandip K. Chakrabarti[2,3⋆]

[1]*Centre for Plasma Astrophysics, Department of Mathematics, K. U. Leuven, Celestijnenlaan 200B, Leuven 3001, Belgium*
[2]*S. N. Bose National Centre for Basic Sciences, JD Block, Sector-III, Salt Lake, Kolkata 700098, India*
[3]*Centre for Space Physics, P61, Southend Garden, Calcutta 700084, India*

Accepted 2003 November 4. Received 2003 October 13; in original form 2003 July 29

ABSTRACT

Matter accreting on to black holes has long been known to have standing or oscillating shock waves. The post-shock matter puffs up in the form of a torus, which intercepts soft photons from the outer Keplerian disc and inverse Comptonizes to produce hard photons. The post-shock region also produces jets. We study the interaction of both hard photons and soft photons, with on-axis electron–positron jets. We show that the radiation from post-shock torus accelerates the flow to relativistic velocities, while that from the Keplerian disc has marginal effect. We also show that the velocity at infinity or the terminal velocity ϑ depends on the shock location in the disc.

Key words: accretion, accretion discs – black hole physics – radiation mechanisms: general – radiative transfer – ISM: jets and outflows.

1 INTRODUCTION

Jets around quasars and microquasars show relativistic terminal speeds. While jets are quite ubiquitous and are associated with a wide range of celestial objects, only some jets around quasars and micro-quasars show highly relativistic terminal speed (e.g. GRS 1915+105, Mirabel & Rodriguez 1994; 3C 273, 3C 345, Zensus, Cohen & Unwin 1995; M87, Biretta 1993). These relativistic jets are generally associated with compact objects and circumstantial evidence shows that many of these central gravitating objects are black holes. Black holes do not have 'hard surfaces' nor do they have atmospheres, hence if observations show that many of these jets come from the vicinity of the black hole, then they must originate from the accretion discs around these black holes.

The inner boundary conditions of matter accreting on to a black hole are (i) supersonic and (ii) sub-Keplerian. Liang & Thompson (1980) showed that sub-Keplerian matter accreting on to a black hole has at least two X-type critical points. In much of the parameter space, it has been shown that supersonic matter crossing the outer critical point undergoes centrifugal pressure-mediated shock (Fukue 1987; Chakrabarti 1989), becomes subsonic and enters the black hole through the inner X-type critical point. Entropy is generated at the shock making the post-shock region hot. The region in which the flow slows down may be extended if the shock conditions are not satisfied. This hot, slowed-down region is puffed up in the form of a torus (hereafter, CENBOL ≡ CENtrifugal pressure-supported BOundary Layer; see Chakrabarti et al. 1996, hereafter, CTKE96). This disc, due to its advection term, may be called an advective accretion disc (Chakrabarti 1989, hereafter C89; Chakrabarti 1990, hereafter C90; Chakrabarti 1996, hereafter C96; CTKE96). Chakrabarti & Titarchuk (1995, hereafter CT95) proposed a disc model which contains both Keplerian matter and sub-Keplerian matter. In this model, the Keplerian matter is of higher angular momentum and low specific energy, and settles around the equatorial plane to form the Keplerian disc (see, Shakura & Sunyaev 1973; Novikov & Thorne 1973, hereafter NT73) while the sub-Keplerian matter with high energy and lower viscosity flanks the cooler Keplerian disc from the top and bottom, sandwiching the Keplerian disc and forming what is known as the sub-Keplerian halo (see, CT95; Chakrabarti 1997, hereafter C97) in the literature. The sub-Keplerian halo may suffer a standing shock at x_s, a few tens of Schwarzschild radii, and it may be sustained there if the post-shock thermal pressure is sufficiently high. The shock compresses the pre-shock flow making it denser and at the same time hotter. In the model solution proposed by Chakrabarti & Titarchuk (CT95), the post-shock region comprises a mixture of the Keplerian and sub-Keplerian components. Thus, though the sub-Keplerian halo (pre-shock) is optically thin for the radiations from the Keplerian disc, the post-shock torus could be optically thin, intermediate, or even thick depending on the Keplerian and sub-Keplerian rates (see CT95, CTKE 96, C97 for details). This is because (1) the Keplerian radiation falls on it at a glancing angle, thereby increasing the path length, and (2) the mixed matter in this region has higher density. CT95 showed that soft radiation from the cool Keplerian disc is inverse-Comptonized by the CENBOL to produce hard radiation. If the sub-Keplerian halo rate ($\dot{M}_h$) is higher, then it supplies more hot electrons to the

⋆E-mail: Indranil.Chattopadhyay@wis.kuleuven.ac.be (IC); sbdas@bose.res.in (SD); chakraba@bose.res.in (SKC)

CENBOL than the soft photons from the Keplerian disc and hence the soft photons cannot cool down the CENBOL significantly. Thus the CENBOL remains puffed up and hot and can intercept a large number of soft photons and inverse-Comptonize them to produce the hard power-law tail of the accretion disc spectrum – a state called the hard state. If, on the other hand, the Keplerian accretion rate ($\dot{M}_K$) is higher, then it supplies more soft photons to cool down the CENBOL region. This results in more power to the soft end of the accretion disc spectrum – a state known as the soft state. Recently, however, Chakrabarti & Mandal (2003) showed that raising the Keplerian rate even higher does not necessarily soften the spectrum, because the Keplerian flow also adds to the number density of electrons in the post-shock region and at some point the spectrum starts to be hardened once more.

This kind of hybrid disc structure is known as the two-component accretion flow or the TCAF disc (see, CT95, CTKE 96, Ebisawa, Titarchuk & Chakrabarti 1996, C97), and has wide observational support (Smith et al. 2001; Smith, Heindl & Swank 2002). In Fig. 1, a schematic diagram of such a disc is presented. The figure shows how the Keplerian disc is sandwiched by the sub-Keplerian halo. The shock location (x_s) and the compact object are also shown. Jets are shown close to the axis of symmetry. Thus jets are illuminated by the Keplerian disc with soft photons and by the CENBOL with hard photons.

Chakrabarti and his collaborators have also shown that the CENBOL can drive a part of the infalling matter along the axis of symmetry to form jets (Chakrabarti 1998, 1999; Das & Chakrabarti 1999; Das et al. 2001). There is wide support that the jets are indeed leaving from a region within 50–100 Schwarzschild radii of the black hole (Junor, Biretta & Livio 1999). Similarly, it is believed that jets are produced only in hard states (see Gallo, Fender & Pooley 2003, and references therein). Thus it is natural to study the interaction of hard radiation from the CENBOL and the outflowing jets, with the particular interest of studying whether momentum deposited onto the jet material by these hard photons can accelerate them to ultrarelativistic speeds.

Investigation of the interaction of radiation and astrophysical flow is not new. A number of astrophysicists have directed their efforts in this particular field of study, while consideration of the associated accretion disc depended on their personal choice or the popularity of the particular model of accretion at the given time. Icke (1980) studied the effect of radiative acceleration of the gas flow above a Keplerian disc. But the effect of radiation pressure on the gas flow was ignored. Sikora & Wilson (1981) showed that even if the jet is collimated by geometrically thick discs (Lynden-Bell 1978; Abramowicz & Piran 1980), radiation drag is important for astrophysical jets. Piran (1982), while calculating the radiative acceleration of outflows about the rotation axis of thick accretion discs, found out that in order to accelerate outflows to $\gamma > 1.5$ (where γ is the bulk Lorentz factor), the funnels must be short and steep, but such funnels are found to be unstable. Sol, Pelletier & Assêo (1989) proposed a two-flow model for jets, one consisting of relativistic particles (electrons and positrons) and of a relativistic Lorentz factor, while the other is a normal, mildly relativistic plasma. In a very important paper, Icke (1989) considered blobby jets about the axis of symmetry of thin discs and he obtained the 'magic speed' of $v_{\rm m} = 0.451c$, where c is the velocity of light, $v_{\rm m}$ being the upper limit of the terminal speed. Fukue (1996) extended this study for rotating flow above a thin disc and drew similar conclusions, although for rotating flow, away from the axis of symmetry, the terminal speed was found out to be a little less than the magic speed of Icke. To summarize, earlier work showed that it is not possible to accelerate jets to ultrarelativistic terminal velocities, by radiation from the earlier accretion disc models. What is more discouraging is the existence of moderate levels of equilibrium speed ($v_{\rm eq}$, i.e. speeds above which there would be radiative deceleration). Recently Fukue, Tojyo & Hirai (2001) have done similar investigations on the interaction of radiation and pair plasma jets, but they took a disc model which consisted of an inner ADAF region (non-luminous) and an outer slim disc (luminous), which resulted in a relativistic terminal speed.

We are working in a different regime, i.e. a less-luminous Keplerian disc and a more-luminous post-shock torus or CENBOL. Since hard radiation is expected to emerge out of the optically thin CENBOL, its intensity (photon counts per unit area per unit time) is low, but it 'looks' directly into the jet vertically above and hence eventually deposits its momentum into the latter. Radiation from a hot CENBOL is likely to be a source of pair-production and hence the possibility of radiative momentum deposition is likely to be higher even for radiation from the CENBOL hitting the outflow at an angle (see, e.g. Yamasaki, Takahara & Kusunose 1999 for the mechanism of pair-production from hot accretion flows). This is why we believe that the direct deposition of momentum may be important.

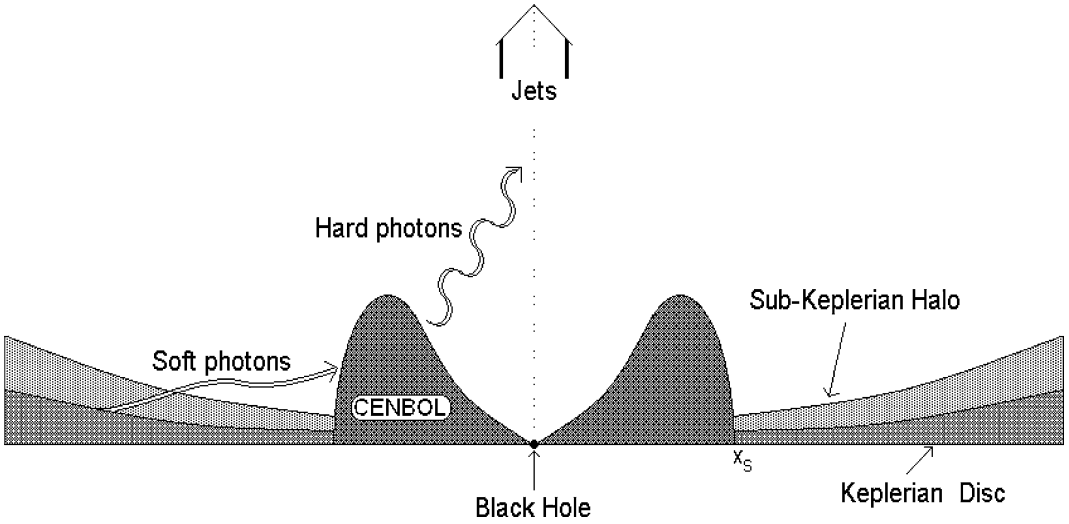

Figure 1. Cross-sectional view of the two-component accretion disc model. Only the top half is shown.

Chattopadhyay & Chakrabarti (2002a) showed that hard radiation from the post-shock region (CENBOL) does accelerate electron–proton plasma to mildly relativistic terminal speeds. Chattopadhyay & Chakrabarti (2002b) also reported that hard radiation from the CENBOL does not impose any upper limit on the terminal speed.

In the present paper, we solve the equations of photo-hydrodynamics of jets for radiation coming out from the TCAF discs, where the radiation fields from both the inner CENBOL and the outer Keplerian thin disc are considered. We show that, while the equilibrium velocity closer to the black hole depends on x_s, and the ratio between the Keplerian disc and the CENBOL luminosities, the terminal speed or the jet velocity at infinity depends on the relative proportions and also on the actual magnitude of various moments of the radiation. We also show that, in hard states (in our parlance, CENBOL radiation dominating over Keplerian radiation), optically thin jets can be accelerated to ultrarelativistic speed.

In the next section, we present the model assumptions and the equations of motion and compute various moments of the radiation field. In Section 3, we present our solutions and finally in Section 4, we draw our conclusions.

2 ASSUMPTIONS, GOVERNING EQUATIONS AND COMPUTATION OF THE MOMENTS OF THE RADIATION FIELD

2.1 Assumptions and governing equations

In our analysis, the curvature effects due to the presence of the central black-hole mass are ignored. The metric is given by $ds^2 = c^2\,dt^2 - dr^2 - r^2\,d\phi^2 - dz^2$, where, r, ϕ, and z are the usual coordinates in cylindrical geometry and ds is the metric in four-space. The four-velocities are u^μ. We follow the convention where the Greek indices signify all four components and the Latin indices represent only the spatial ones. The black hole is assumed to be non-rotating and hence the strong gravity is taken care of by the so-called Paczynski–Wiita potential (e.g. Paczynski & Wiita 1980).

We also do not consider the generation mechanism of the jets. As the astrophysical jets are observed to be extremely collimated (Bridle & Perley 1984), and generally aligned along the normal to the host galaxy, we assume the jet to be along the axis of symmetry. Thus the transverse structure of the jet is ignored, i.e. $u^r = u^\phi = 0$ and $\partial/\partial r = \partial/\partial\phi = 0$, where u^r and u^ϕ are the radial and azimuthal components of the four-velocity. We are looking for steady-state solutions. Hence, $\partial/\partial t = 0$. We also assume the gas pressure is negligible compared to the radiation pressure. This is perhaps the case especially inside the funnel wall close to the axis. The derivation of the equations of motion of radiation hydrodynamics for an optically thin plasma was investigated by a number of workers. A detailed account of such derivations has been presented by Mihalas & Mihalas (1984, hereafter MM84) and Kato, Fukue & Mineshige (1998, hereafter K98), and they are not presented here. Enforcing the above assumptions, the equation of motion presented in MM84 and K98 reduces to

$$u^z\frac{du^z}{dz} = -\frac{GM_B}{(z-2)^2} + \frac{\sigma_T}{m}\left[\gamma\frac{F^z}{c} - \gamma^2 E u^z - u^z P^{zz} + u^z\left(2\gamma u^z\frac{F^z}{c} - u^z u^z P^{zz}\right)\right],$$

where u^z is the z-component of the four-velocity, G, M_B, σ_T, and m are the universal gravitation constant, the mass of the black hole, the Thomson scattering cross-section and the mass of the gas particle, respectively. E, F^z and P^{zz} are the radiative energy density, radiative flux and radiative pressure on the axis of symmetry, and γ ($\gamma = u_t$) is the Lorentz factor. The above equation can be rewritten as

$$u^z\frac{du^z}{dz} = -\frac{GM_B}{(z-2)^2} + [\gamma\mathcal{F} - \gamma^2\mathcal{E}u^z - u^z\mathcal{P} + u^z(2\gamma u^z\mathcal{F} - u^z u^z\mathcal{P})], \quad (1)$$

where

$$\mathcal{E} = \frac{\sigma_T}{m}E,\ \mathcal{F} = \frac{\sigma_T}{mc}F^z \quad \text{and} \quad \mathcal{P} = \frac{\sigma_T}{m}P^{zz}.$$

For simplicity, we will not compute the shock location x_s or the CENBOL luminosity (L_C) – instead, we will supply them as free parameters. They can be easily computed from accretion parameters (e.g. C89, CT95, Das et al. 2001; Chattopadhyay et al. 2003). We assume that the outflow is made up of purely electron–positron pair plasma.

2.2 Computation of radiative moments from the TCAF disc

The radiation reaching each point on the jet axis comes from two parts of the disc, namely, the CENBOL and the Keplerian disc, hence all the radiative moments should have both contributions.

In Fig. 2, a schematic diagram of the cross-section of the disc structure is presented. The black hole is situated at O. The region bounded between O and x_s is the CENBOL, and the thick line between x_s and x_o is the Keplerian disc, where x_o is the outer boundary of the Keplerian disc. Thus x_s is the outer boundary of the CENBOL and the inner boundary of the Keplerian disc. The inner boundary of the Keplerian disc, as seen from position B, is x_{Ki}. The shock height is $h_s \sim a_s x_s^{1/2}(x_s - 1)$, where a_s is the equatorial sound speed at the shock and depends on x_s. In other words $h_s = h_s(x_s)$, but as we are not solving the accretion disc equations simultaneously, we have to make some estimate of h_s which will closely mimic reality. The solutions of Chakrabarti (C89, C90, CT95, C96) show that if $x_s = 10r_g$, where r_g is the Schwarzschild radius, then the temperature at the shock is $T_{10} \sim 1.56 \times 10^{11} K$. Assuming that the shock temperature is $T_s = T_{10}(10/x_s)$, one can estimate the shock height to be $h_s \sim 0.6(x_s - 1)$. The inner surface of the CENBOL is assumed to be conical. The radiations from a point $D(r', z')$ on the surface of the CENBOL is primarily along the local normal **DC**. Similarly, the radiation from a point $D'(r'_K, 0)$ on the Keplerian disc is along its local normal $\mathbf{D'C'}$.

The radiative moments at B are

$$E = \frac{1}{c}\int I\,d\Omega = \frac{1}{c}\left(\int_C I_C\,d\Omega_C + \int_K I_K\,d\Omega_K\right), \quad (2a)$$

$$\frac{F^i}{c} = \frac{1}{c}\int I l^i\,d\Omega = \frac{1}{c}\left(\int_C I_C l^i_C\,d\Omega_C + \int_K I_K l^i_K\,d\Omega_K\right), \quad (2b)$$

and

$$P^{ij} = \frac{1}{c}\int I l^i l^j\,d\Omega = \frac{1}{c}\left(\int_C I_C l^i_C l^j_C\,d\Omega_C + \int_K I_K l^i_K l^j_K\,d\Omega_K\right). \quad (2c)$$

In equations (2a)–(2c), I is the frequency integrated intensity from the disc, d Ω is the differential solid angle at B and l^i are the direction cosines at B, for example $l^z_C = (z - z')/BD$ and $l^z_K = z/BD'$.

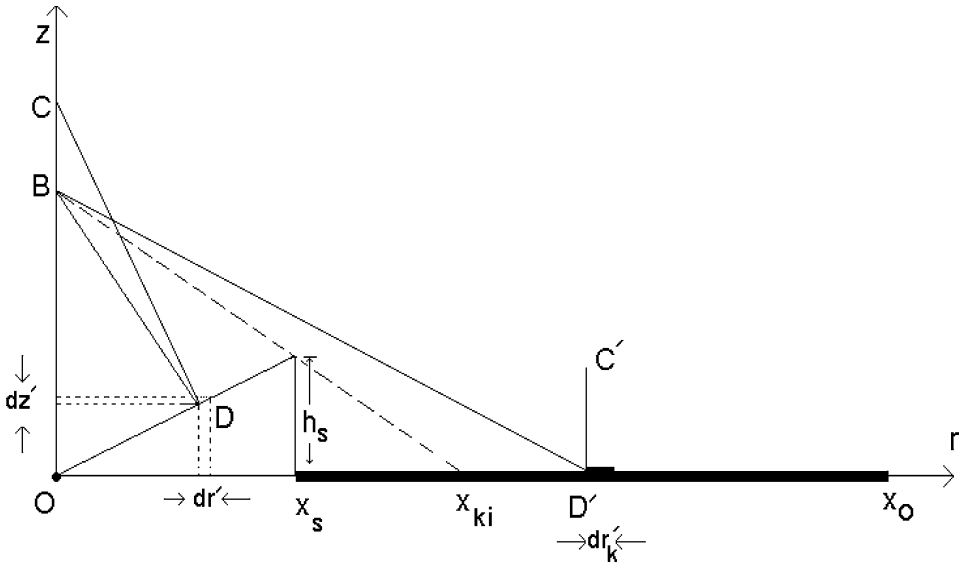

Figure 2. Schematic diagram of a two-component accretion flow (TCAF). O is the position of the black hole. The centrifugal pressure-dominated boundary layer (CENBOL) is the puffed up region between O and x_s, the shock location. The thick line between x_s and x_o is the Keplerian disc where x_o is the outer boundary of the Keplerian disc. **DC** and **D′C′** are the local normals of the CENBOL and Keplerian disc. $B(0, z)$ is the field point where various moments of the radiation fields are computed. $D(r', z')$ is the source point on the CENBOL and $D'(r'_K, 0)$ is the source point on the Keplerian disc. r' is the radial coordinate of the CENBOL and r'_K is that of the Keplerian disc. The sub-Keplerian halo is not shown.

The suffixes C and K represent quantities linked to the CENBOL and the Keplerian disc respectively. The expressions of solid angles subtended at B from D and D' are given respectively by

$$\mathrm{d}\Omega_C = \frac{r'\mathrm{cosec}\theta\ \mathrm{d}r'\ \mathrm{d}\phi}{r'^2 + (z - z')^2} \cos(\angle CDB), \tag{3a}$$

and

$$\mathrm{d}\Omega_K = \frac{r'_K\ \mathrm{d}r'_K\ \mathrm{d}\phi}{r'^2_K + z^2} \cos(\angle C'D'B), \tag{3b}$$

where θ is the semivertical angle of the inner surface of the CENBOL which, for simplicity, is assumed to be constant. It is to be noted that, from Fig. 2 and equations (3a)–(3b), in general, $l^z_C > l^z_K$ and for any unit differential area on the disc, $\mathrm{d}\Omega_C > \mathrm{d}\Omega_K$. This implies that the contribution from the CENBOL to the total radiation field moment is much greater, compared to that from the Keplerian disc. This will be clear when the comparative study of the moments is presented later (see Fig. 3).

It is clear from equation (2b) that, due to the symmetry about the z-axis, the only non-zero pressure tensor components are P^{ii} and $F^r = F^\phi = 0$ on the axis. Only F^z is non-zero. As we consider jets on or about the axis of symmetry and the transverse structure is ignored, P^{rr} and $P^{\phi\phi}$ do not enter the equation of motion as these components are only coupled with $u^r(=0)$ and $u^\phi(=0)$, i.e. we have only to compute P^{zz}, which is exactly what is seen in equation (1).

From Fig. 2, it is clear that for the outflowing matter within the funnel, i.e. when $z < [h_s x_o/(x_o - x_s)]$, radiation from the Keplerian disc does not reach the electrons because this radiation is intercepted by the CENBOL. The CENBOL will reprocess these intercepted photons, and re-emit them in all directions, especially towards the jets because of the special geometry and directiveness of the CENBOL surface. Due to the shadowing effect mentioned above, the radiation from the Keplerian disc reaching B is from x_{Ki} to x_o, where $x_{Ki} = x_s z/(z - h_s)$, with the additional constraints, $x_s \leqslant x_{Ki} \leqslant x_o$ and $x_{Ki} > 0$.

As far as the CENBOL properties are concerned, we follow CT95, where an effective temperature was computed for the CENBOL and the radiation intensity was chosen to be uniform. That is $I_C = L_C/\pi\mathcal{A} = \ell L_{Edd}/\pi\mathcal{A} =$ constant, where L_C and $\mathcal{A}$ are the CENBOL luminosity and the surface area of the CENBOL, respectively. L_{Edd} is the Eddington luminosity and ℓ is the CENBOL luminosity in units of L_{Edd}. The Keplerian disc intensity per unit solid angle is

$$I_K = \frac{3GM_B\dot{M}_K}{8\pi^2 r_K^3}\left(1 - \sqrt{\frac{3r_g}{r_K}}\right) \quad \text{(NT73)}.$$

Let us now multiply σ_T/m with equations (2a)–(2c), and then integrate over the whole disc to obtain the following integrated quantities for the moments:

$$\begin{aligned}\mathcal{E} &= \mathcal{E}_{K0}\int_{x_{Ki}}^{x_o} \frac{2\pi z\left[r'^{-2}_K - \sqrt{3}r'^{-5/2}_K\right]\mathrm{d}r'_K}{\left(z^2 + r'^2_K\right)^{3/2}} \\ &\quad + \mathcal{E}_{C0}\int_{r_{in}}^{x_s} \frac{2\pi\cot\theta\{r' + (z - r'\cot\theta)\tan\theta\}r'\,\mathrm{d}r'}{[(z - r'\cot\theta)^2 + r'^2]^{3/2}} \\ &= \mathcal{E}_{K0}\tilde{E}_K(z, x_s, x_o) + \mathcal{E}_{C0}\tilde{E}_C(z, r_{in}, x_s) \\ &= \mathcal{E}_K + \mathcal{E}_C,\end{aligned} \tag{4a}$$

where r_{in} is the inner boundary of the disc.

$$\begin{aligned}\mathcal{F} &= \mathcal{F}_{K0}\int_{x_{Ki}}^{x_o} \frac{2\pi z\left[r'^{-2}_K - \sqrt{3}r'^{-5/2}_K\right]z\,\mathrm{d}r'_K}{\left(z^2 + r'^2_K\right)^2} \\ &\quad + \mathcal{F}_{C0}\int_{r_{in}}^{x_s} \frac{2\pi\cot\theta\{r' + (z - r'\cot\theta)\tan\theta\}r'(z - r'\cot\theta)\,\mathrm{d}r'}{[(z - r'\cot\theta)^2 + r'^2]^2} \\ &= \mathcal{F}_{K0}\tilde{F}_K(z, x_s, x_o) + \mathcal{F}_{C0}\tilde{F}_C(z, r_{in}, x_s) \\ &= \mathcal{F}_K + \mathcal{F}_C\end{aligned} \tag{4b}$$

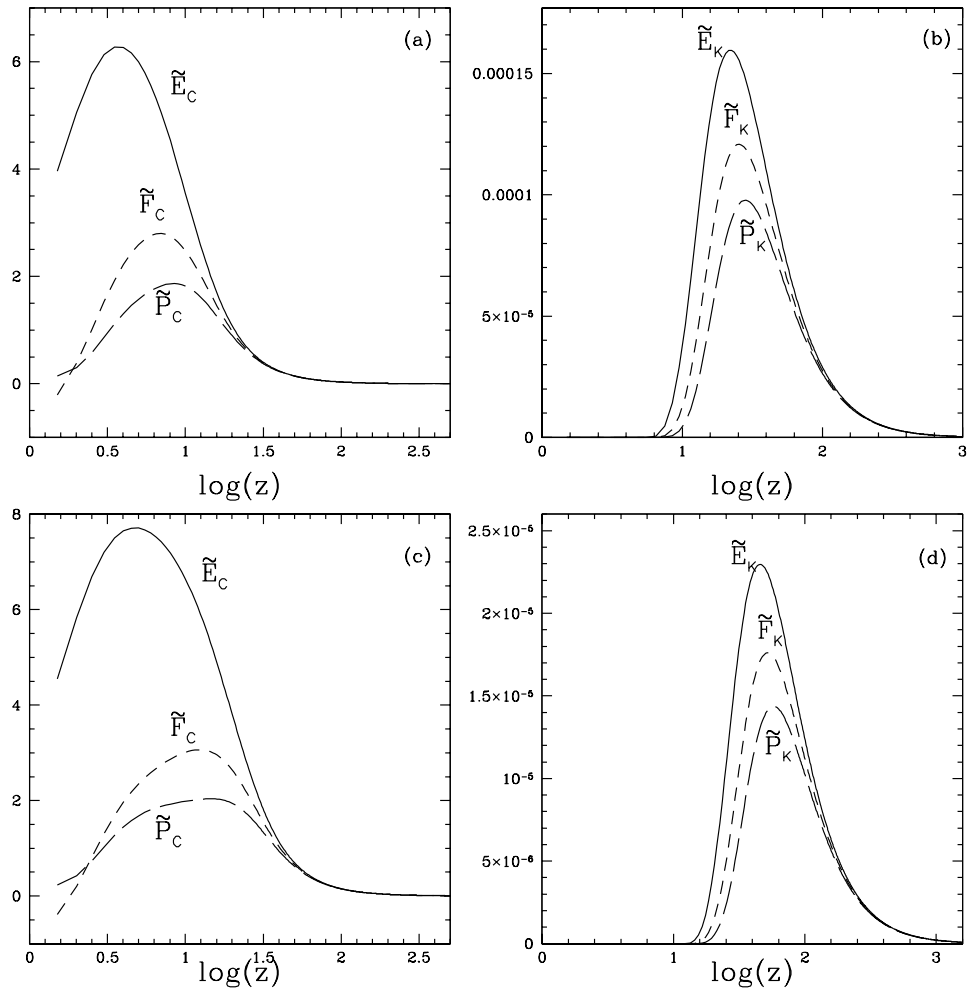

Figure 3. Variations of the spatial part of the radiation moments, $\tilde{E}$ (solid) $\tilde{F}$ (dashed) and $\tilde{P}$ (long-dashed) with $\log(z)$. (a) Contributions from the CENBOL denoted by suffix C, and (b) contributions from the Keplerian disc denoted by suffix K; the shock location is $x_s = 10r_g$. (c) Contributions from the CENBOL for $x_s = 20r_g$, and (d) contributions from the Keplerian disc for $x_s = 20r_g$. The suffixes have the same meaning as in the previous two figures.

$$\mathcal{P} = \mathcal{P}_{K0}\int_{x_{Ki}}^{x_o}\frac{2\pi z\left[r_K'^{-2}-\sqrt{3}r_K'^{-5/2}\right]z^2\,dr_K'}{\left(z^2+r_K'^2\right)^{5/2}} + \mathcal{P}_{C0}\int_{r_{in}}^{x_s}\frac{2\pi\cot\theta\{r'+(z-r'\cot\theta)\tan\theta\}r'(z-r'\cot\theta)^2\,dr'}{[(z-r'\cot\theta)^2+r'^2]^{5/2}}$$
$$= \mathcal{P}_{K0}\tilde{P}_K(z,x_s,x_o)+\mathcal{P}_{C0}\tilde{P}_C(z,r_{in},x_s)$$
$$= \mathcal{P}_K+\mathcal{P}_C \qquad (4c)$$

The constancy of I_C allows us to have analytical expressions for $\tilde{E}_C$, $\tilde{F}_C$ and $\tilde{P}_C$. These were computed by Chattopadhyay & Chakrabarti (2000, 2002a,b) and are not repeated here. We choose the unit of length to be $2GM_B/c^2$ (the Schwarzschild radius r_g), the unit of time to be $2GM_B/c^3$ and M_B to be the unit of mass. Thus the unit of velocity is c. In such units, the constants in equations (4a)–(4c) are

$$\mathcal{E}_{C0} = \mathcal{F}_{C0} = \mathcal{P}_{C0} = \frac{1.3\times10^{38}\ell\sigma_T}{2\pi cm\mathcal{A}G\,M_\odot} \qquad (5a)$$

and

$$\mathcal{E}_{K0} = \mathcal{F}_{K0} = \mathcal{P}_{K0} = \frac{4.32\times10^{17}\dot{m}_k\sigma_T c}{32\pi^2 mG\,M_\odot}. \qquad (5b)$$

We have written the Keplerian accretion rate in units of the Eddington accretion rate $\dot{M}_{Edd}$, i.e. $\dot{m}_K = \dot{M}_K/\dot{M}_{Edd}$. It is to be noted that two of the disc parameters, i.e. $r_{in} = 1.5r_g$ and $x_o = 1000r_g$ are kept constant throughout the paper. In Fig. 3, the space-dependent part of the moments $\tilde{E}$, $\tilde{F}$ and $\tilde{P}$ are compared for two shock locations. In Figs 3(a) and (b), the contributions from the CENBOL and the Keplerian disc are plotted for $x_s = 10r_g$ and in Figs 3(c) and (d) the contributions from the CENBOL and the Keplerian disc are plotted, where the shock location is $x_s = 20r_g$. We see that as x_s is increased, the CENBOL contributions increase while the Keplerian contributions decrease. We also see another fact that generally, in the hard state, the CENBOL contribution to the total radiative moments dominates over the Keplerian counterparts. We see from Figs 3(a) and (c) that within the funnel (i.e. $z \leqslant h_s$), $\tilde{E}_C > \tilde{F}_C > \tilde{P}_C$. We also see that, because of the relatively small size of the CENBOL, $\tilde{E}_C \approx \tilde{F}_C \approx \tilde{P}_C$ for smaller values of z, e.g. $z \sim 50.5r_g$ for Fig. 3(a) and $z \sim 92.5r_g$ for Fig. 3(c), while we see $\tilde{E}_K \approx \tilde{F}_K \approx \tilde{P}_K$ at much larger distances, e.g. $z \sim 900r_g$ for Fig. 3(b) and $z \sim 1500r_g$ for Fig. 3(d). The small size of the CENBOL ensures that the direction cosines $l_C^z \to 1$ for smaller z. In contrast, the larger size of the Keplerian disc ensures $l_K^z \sim 1$ only for large z. From Figs 3(a)–(d) it appears that as $\tilde{E}_C \gg \tilde{E}_K$, $\tilde{F}_C \gg \tilde{F}_K$, and $\tilde{P}_C \gg \tilde{P}_K$. So, if the CENBOL is more luminous, then CENBOL contributions would dominate the

Keplerian contributions even at large z. While $\mathcal{E}_{K0}$ ($=\mathcal{F}_{K0}=\mathcal{P}_{K0}$) depends only on $\dot{m}_K$, $\mathcal{E}_{C0}$ ($=\mathcal{F}_{C0}=\mathcal{P}_{C0}$) depends on both ℓ and the CENBOL surface area. From Figs 3(a) and (c), we see that with the increase of x_s, even if the radiative moments from the CENBOL, say for example, $\tilde{E}_C$ increases moderately, calculations show that $\tilde{E}_{C0}$ decreases appreciably with x_s (e.g. $\tilde{E}_{C0}$ for $x_s = 10r_g$ is about four times larger than $\tilde{E}_{C0}$ for $x_s = 20r_g$). So Keplerian contributions might be comparable to that due to the CENBOL at large z, depending on the specific combinations of all the parameters ℓ, $\dot{m}_K$ and x_s, especially for large values of x_s and low ℓ. We also observe that the shadow effect of the CENBOL ensures that $\tilde{E}_K = \tilde{F}_K = \tilde{P}_K = 0$ at $z \leqslant (h_s x_o)/(x_o - x_s)$.

3 RADIATIVE ACCELERATION

In the rest of the paper, we will use the geometrical units defined in the last section, but for simplicity we will keep the same symbols representing variables as in equation (1). We define a three-velocity v such that $v^2 = -u_i u^i/u_t u^t = -u_z u^z/u_t u^t$. Thus $u^z = \gamma v$ and $u_z = -\gamma v$. Under such considerations equation (1) takes the form,

$$\frac{\mathrm{d}v}{\mathrm{d}z} = \frac{-\frac{1}{2(z-1)^2} + [\gamma\mathcal{F} - \gamma^3 v\mathcal{E} - \gamma v\mathcal{P} + \gamma^3(2v^2\mathcal{F} - v^3\mathcal{P})]}{\gamma^4 v}. \quad (6)$$

The first term on the right-hand side of equation (6) is the gravitational term with dimensionless Paczynski–Wiita potential and the term in the square brackets is the radiative acceleration term. We notice that the radiative acceleration term depends both on v and the radiative moments. The first and fourth terms in the square brackets are accelerating terms while the second, third and fifth terms are the decelerating terms, collectively known as the radiation drag terms. We also see that there is a γ^4 term in the denominator of the right-hand side of equation (6). This term ensures that, apart from radiation drag, outflowing matter will be slowed down as $v \to 1$.

3.1 Equilibrium velocity

Let us now discuss the concept of equilibrium velocity. As a concept, equilibrium velocity is not new and has been extensively discussed by a number of astrophysicists (see, Fukue 2003, and references therein for details). We want to study this issue in the context of jets in the radiation field of TCAF discs. It is defined in a manner that at $v = v_{eq}$ the square-bracket term in equation (6) is zero. Thus, for $v > v_{eq}$ there is deceleration and for $v < v_{eq}$ there is radiative acceleration.

Putting the square-bracket term in equation (6) to zero we have

$$\mathcal{F}v_{eq}^2 - (\mathcal{E}+\mathcal{P})v_{eq} + \mathcal{F} = 0. \quad (7)$$

This is a quadratic equation in v_{eq} whose solution is

$$v_{eq}(z) = \frac{(\mathcal{E}+\mathcal{P}) - \sqrt{(\mathcal{E}+\mathcal{P})^2 - 4\mathcal{F}^2}}{2\mathcal{F}} = \xi - \sqrt{(\xi^2-1)}, \quad (8)$$

where $\xi = (\mathcal{E}+\mathcal{P})/2\mathcal{F}$. From equations (4a)–(5b), we have

$$\xi(z) = \frac{(\tilde{E}_C + \tilde{P}_C) + (\dot{m}_K/\ell)\zeta(\tilde{E}_K + \tilde{P}_K)}{2(\tilde{F}_C + (\dot{m}_K/\ell)\zeta\tilde{F}_K)}, \quad (9)$$

where $\zeta = 6.6\times10^{-13}c^2\mathcal{A}$. It is to be noted that ξ depends on x_s as well as on the ratio $\dot{m}_K/\ell$, but not separately on $\dot{m}_K$ and ℓ. In case $(\dot{m}_K\zeta)/\ell \ll 1$, v_{eq} is completely determined by $\tilde{E}_C$, $\tilde{F}_C$ and $\tilde{P}_C$, and ℓ has no effect in determining v_{eq}. We also see that ξ does not depend on the mass of the gas particles m. Thus ξ (and thus v_{eq}) is the same for both an electron–proton plasma as well as an electron–positron plasma, provided x_s and $\dot{m}_K/\ell$ is the same in both cases. It is clear from equations (8) and (9) that as $\mathcal{E} \approx \mathcal{F} \approx \mathcal{P}$, $v_{eq} \to 1$. Therefore if the CENBOL contribution dominates then $v_{eq} \sim 1$ within a few tens of Schwarzschild radii above the disc plane. If Keplerian radiation dominates, then the condition is achieved at much larger distance, as we shall see later. We also see that no outflow is possible, i.e. $v_{eq} \leqslant 0$, that is if

$$\mathcal{F} \leqslant 0. \quad (10)$$

From Fig. 3 we see that very close to the horizon, due to the torus geometry of the CENBOL, $\mathcal{F} < 0$, hence very close to the black hole, not only enormous gravitational pull but also the radiative force pushes matter inward.

Icke's magic speed

Let us now recover an important result from equation (8). If we consider a thin-Keplerian disc of infinite size, then $P_K^{zz} = P_K^{rr} = P_K^{\phi\phi} = \frac{1}{3}E_K$ and $F_K^z = \frac{c}{2}E_K$, and there is no CENBOL in this particular case. Under such conditions $\mathcal{E} = 2\mathcal{F} = 3\mathcal{P}$, and putting these in equation (8) we have

$$v_{eq} = v_m = \frac{1}{3}(4-\sqrt{7}) = 0.451 \equiv \text{the magic speed of Icke!}$$

Thus we see that, if the radiation field, i.e. the radiative properties of the disc, can be prescribed, then v_{eq} can be found easily.

Equilibrium speed from a TCAF disc

Let us now concentrate on the radiation from TCAF discs. As discussed in the introduction, jets are produced in the hard state of the accretion disc when the CENBOL is hotter and the hard state means more power is on the high-energy end of the spectrum. That is, $L_C > L_K$. The Keplerian disc luminosity is given by

$$L_K = r_g^2 \int_{x_s}^{x_o} 2\pi I_K 2\pi r_K \, \mathrm{d}r_K,$$

which is a function of $\dot{m}_K$, x_s and x_o, which when integrated can be expressed as,

$$L_K = r_g^2 \int_{x_s}^{x_o} 2\pi I_K 2\pi r_K \, \mathrm{d}r_K = \frac{3}{4}\dot{m}_K \left[-\frac{1}{r_K} + \frac{2}{3r_K}\sqrt{\frac{3}{r_K}}\right]_{x_s}^{x_o} L_{Edd}. \quad (11)$$

Thus the Keplerian disc luminosity in units of the Eddington luminosity can be defined as $\ell_K = L_K/L_{Edd}$. As has been stated before, presently we do not compute L_C, but supply it. Typical values of ℓ that we shall employ should, in general, depend on ℓ_K itself because $\ell \sim \Lambda\ell_K$, where Λ is the enhancement factor by which the incident photon intensity is increased due to Comptonization and has a value of around 20–30 in hard states (CT95). Thus, for instance, if $\ell_K \sim 0.05$, a typical value of ℓ is about 0.1–0.15. However, while we shall choose ℓ and ℓ_K in these regions, we shall use them as free parameters, since at present we are not interested in computing the terminal speed as a function of the spectral slope α, though, strictly speaking, it would be a function of α.

In our case, we see that there are two sources of radiation from the disc: (i) the CENBOL and (ii) the Keplerian disc. Let us first

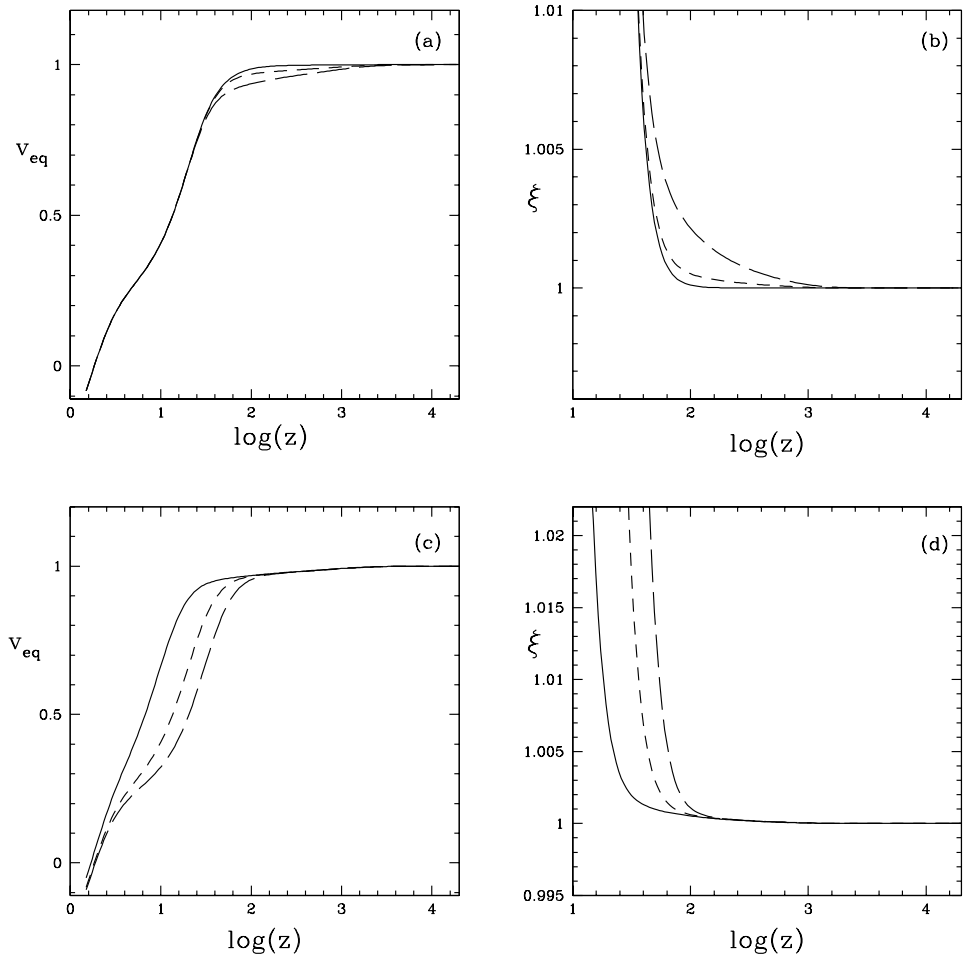

Figure 4. Variation of (a) $v_{\rm eq}$ and (b) ξ with log(z) for $\ell = 0.3$ and $x_{\rm s} = 20r_{\rm g}$. The various curves correspond to $\dot{m}_{\rm K} = 0.01$ (solid), $\dot{m}_{\rm K} = 1$ (dashed) and $\dot{m}_{\rm K} = 6$ (long-dashed). Variation of (c) $v_{\rm eq}$ and (d) ξ with log(z) for $\ell = 0.12$ and $\dot{m}_{\rm K} = 0.5$. The various curves correspond to $x_{\rm s} = 10\ r_{\rm g}$ (solid), $x_{\rm s} = 20r_{\rm g}$ (dashed) and $x_{\rm s} = 30r_{\rm g}$ (long-dashed).

concentrate on the CENBOL contribution. From Figs 3(a) and (c), we see that for $z \rightarrow$ few $\times\ 10r_{\rm g}$, $(\mathcal{E}_{\rm C}+\mathcal{P}_{\rm C}) \sim 2\mathcal{F}_{\rm C}$, hence equation (8) determines $v_{\rm eq} \sim 1$ at such distances.

In general, in the hard state also, $L_{\rm K}$ is not negligible. Though as z becomes large, $\tilde{E}_K \approx \tilde{F}_K \approx \tilde{P}_K$, but at $z \sim$ few $\times\ 10r_{\rm g}$, $(\mathcal{E}_{\rm K} + \mathcal{P}_{\rm K}) > 2\mathcal{F}_{\rm K}$. Hence for higher Keplerian luminosity, $v_{\rm eq} \sim 1$ is achieved at distances around a thousand Schwarzschild radii. In Figs 4(a) and (b), we have plotted $v_{\rm eq}$ and ξ against log(z). The various curves correspond to $\dot{m}_{\rm K} \sim 0.01$ (solid), $\dot{m}_{\rm K} = 1$ (dashed) and $\dot{m}_{\rm K} = 6$ (long-dashed). We choose $\ell = 0.3$ and $x_{\rm s} = 20r_{\rm g}$ for all the plots. We see that close to the black hole, $v_{\rm eq}$ is independent of $\ell_{\rm K}$, because at such distances radiation from the CENBOL dominates. If $L_{\rm C} \gg L_{\rm K}$ (i.e. solid curve), then we see that $v_{\rm eq} \rightarrow 1$ at around $100r_{\rm g}$. For $\dot{m}_{\rm K} = 1$ ($\equiv \ell_{\rm K} \sim 0.03$, i.e. dashed curve), and for $\dot{m}_{\rm K} = 6$ (i.e. long-dashed curve), $v_{\rm eq} \rightarrow 1$ at distances over 1000 $r_{\rm g}$. One should note that at $z < 1.85r_{\rm g}$, $v_{\rm eq} < 0$. The reason for this can be clearly seen from Fig. 3(c), which shows that $\mathcal{F} < 0$ at the same distance from the black hole. This means that, very close to the black hole, not only does gravity push in matter but also radiation would also push matter inside, thus vindicating equation (10). To clarify this point we have plotted ξ against log(z) in Fig. 4(b). The curve styles match those of the corresponding case in Fig. 4(a). We see that within the funnel-like region of the CENBOL, the radiation is completely dominated by the CENBOL itself, and also due to this particular geometry $\xi > 1$, resulting in $v_{\rm eq}$ being much smaller than the velocity of light. In case $\dot{m}_{\rm K}$ becomes small (solid), for $z > 100r_{\rm g}$, $\xi \rightarrow 1$, resulting in $v_{\rm eq} \rightarrow 1$. In case $\dot{m}_{\rm K}$ becomes large (dashed and long-dashed curves), $\xi \sim 1$ only at around a thousand Schwarzschild radii. This means that, if one increases $\dot{m}_K$, then the higher velocities achieved due to the acceleration of jets by CENBOL photons might be decelerated. It is quite obvious, though, that the effect of Keplerian radiation is quite marginal. Of course one should keep in mind that if the radiative moments due to CENBOL and Keplerian radiation are comparable at infinite distances, then there is a possibility of increased terminal speed, with the increase in $\dot{m}_K$.

We have seen from equation (9) that ξ not only depends on $\dot{m}_K/\ell$ but also on $x_{\rm s}$. We now investigate the dependence of $v_{\rm eq}$ on $x_{\rm s}$. In Fig. 4(c), $v_{\rm eq}$ is plotted against log (z) for $\ell = 0.12$ and $\dot{m}_K = 0.5$. The various curves represent $x_{\rm s} = 10r_{\rm g}$ (solid), $x_{\rm s} = 20r_{\rm g}$ (dashed) and $x_{\rm s} = 30r_{\rm g}$ (long-dashed). With the increase in $x_{\rm s}$, as the size of the CENBOL increases – hence it can only behave like a point source (for which $\xi \rightarrow 1$) farther out – and we see that $v_{\rm eq} \rightarrow 1$ farther out from the black hole. To clarify this, we have also plotted ξ against log(z) for $\ell = 0.12$ and $\dot{m}_K = 0.5$ in Fig. 4(d). The various curves represent $x_{\rm s} = 10r_{\rm g}$ (solid), $x_{\rm s} = 20r_{\rm g}$ (dashed) and $x_{\rm s} = 30r_{\rm g}$ (long-dashed). As has just been explained, we see that $\xi \rightarrow 1$ for larger values of z, as $x_{\rm s}$ is increased.

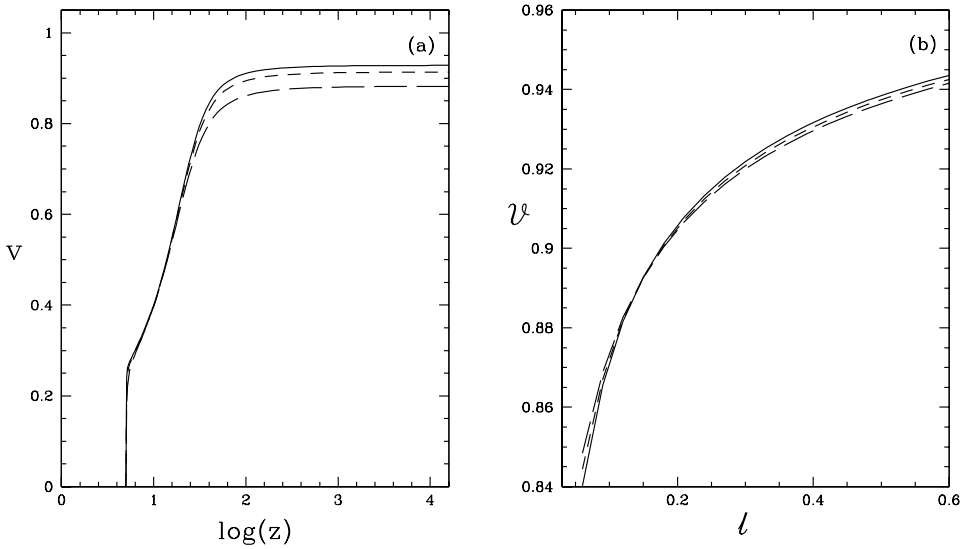

Figure 5. (a) Variation of v with $\log(z)$, for $\dot{m}_K = 0.5$. The various curves correspond to $\ell = 0.36$ (solid), $\ell = 0.24$ (dashed) and $\ell = 0.12$ (long-dashed). (b) Variation of ϑ with ℓ. The various curves correspond to $\dot{m}_K = 0.4$ (solid), $\dot{m}_K = 1.4$ (dashed) and $\dot{m}_K = 2.4$ (long-dashed). The shock location is $x_s = 20r_g$ for both cases. The injection parameters are $z_{in} = 5r_g$, $v_{in} = 10^{-3}$.

3.2 Velocity profile

So far, we have only discussed the equilibrium velocity and its dependence on ℓ, $\dot{m}_K$ and x_s. This was done to study the upper limit of the allowed velocity as a function of z. We have seen that if the CENBOL radiation dominates over that from the Keplerian disc, then jets can be accelerated to very high velocities within around $100r_g$, but v_{eq} is only a measure of velocity which signifies only the domain of radiative deceleration or acceleration, and is not the actual velocity. From equation (6) it is quite clear that the radiative acceleration and hence v itself depends on all three quantities $\mathcal{E}, \mathcal{F}, \mathcal{P}$ and not just on ξ. Equation (6) also shows that radiative acceleration also depends on v in a very complicated way. To compute the actual velocity, one has to integrate equation (6). Jets are believed to be produced from the post-shock region (Chakrabarti 1999; Das & Chakrabarti 1999; Das et al. 2001). If they are generated from the post-shock region then they should start with very small velocity. In this paper we are not concentrating on the generation of jets. Thus we just put the injection height to be close to the black hole and the injection velocity to be small. We choose injection parameters to be $z_{in} = 5r_g$ and $v_{in} = 10^{-3}$. Before discussing the results, let us define the terminal speed. The terminal speed (ϑ) is the constant velocity at infinite distances or $\vartheta = v|_{z\to\infty}$. In Fig. 5(a), the three-velocity v is plotted against $\log(z)$, where $\dot{m}_K = 0.5$ and $x_s = 20r_g$. The various curves correspond to $\ell = 0.36$ (solid), $\ell = 0.24$ (dashed) and $\ell = 0.12$ (long-dashed). We see that close to the black hole as $v \ll 1$, $\mathcal{F}$ dominates resulting in a steep rise in v; as v increases the jet starts to feel the drag force, resulting in a somewhat less steep increase in v. At $z > 100r_g$, the radiative moments tend to become weak and the jet settles to a constant velocity at large z or the terminal speed ϑ. It is clear that v increases with ℓ and in the three cases depicted, the terminal velocities of jets are $\vartheta \sim 0.93$ (solid), $\vartheta \sim 0.91$ (dashed) and $\vartheta \sim 0.88$ (long-dashed). It may seem curious that even if ℓ is increased by equal intervals the terminal speed achieved does not increase by equal intervals. The reason is two-fold: first of all, from equation (6), one can see that the gradient of v is a non-linear function of the moments. The second reason is the existence of the γ^4 term in equation (6), which suppresses the acceleration, as v increases to values close to that of light.

In Fig. 5(b), the terminal speed ϑ is plotted with ℓ, for $x_s = 20r_g$. The various curves correspond to $\dot{m}_K = 0.4$ (solid), $\dot{m}_K = 1.4$ (dashed) and $\dot{m}_K = 2.4$ (long-dashed). The terminal speed ϑ increases with ℓ, though for higher ℓ, the increase of ϑ decreases, for the same two reasons discussed for the previous figure. We also see that the dependence of ϑ on $\dot{m}_K$ is marginal. In Fig. 3, we have seen that the CENBOL contribution to the various space-dependent parts of the radiative moments is a few orders of magnitude higher than that from the Keplerian contribution, hence the marginal dependence of ϑ with $\dot{m}_K$ is expected. It is to be noted, though, that for $\ell > 0.15$, ϑ decreases with increasing $\dot{m}_K$ and for $\ell < 0.15$, ϑ increases with increasing $\dot{m}_K$, albeit the dependence is very weak. For the higher values of ℓ, the jet, powered by the CENBOL radiation, achieves a very high velocity within a few tens of Schwarzschild radii. But for the next thousand Schwarzschild radii or so, $\xi > 1$, as $(\mathcal{E}_K + \mathcal{P}_K) > 2\mathcal{F}_K$ in that region – see Figs 3(c) and (d). When v becomes high, the drag force increases, and slows down the jet. At a larger distance, a slight increase in radiative moments, due to the increase in $\dot{m}_K$, is not sufficient to increase ϑ. When ℓ is small, the velocity achieved within few tens of Schwarzschild radii is not that high, hence the drag force is less. But at large distances, the radiative moments due to the CENBOL and Keplerian disc becomes comparable hence there is a slight increase in ϑ with $\dot{m}_K$.

In Fig. 6, ϑ is plotted against $\dot{m}_K$, for $x_s = 20r_g$. The various curves correspond to $\ell = 0.3$ (solid), $\ell = 0.24$ (dashed), $\ell = 0.18$ (long dashed) and $\ell = 0.12$ (dashed-dotted). We see that, as in Fig. 5(b), for higher ℓ, ϑ decreases with increasing $\dot{m}_K$ (see the solid, dashed and long-dashed curves), but for lower values of ℓ, ϑ increases with increasing $\dot{m}_K$ (see the dashed-dotted curve). So one can conclude that in the hard state, jets are basically accelerated by radiation from the CENBOL and the terminal velocity has a weak dependence on radiation from Keplerian disc.

Let us now investigate the dependence on x_s. In Fig. 7(a), v is plotted against $\log(z)$, for $\ell = 0.18$ and $\dot{m}_K = 0.5$. The various curves correspond to $x_s = 10r_g$ (solid), $x_s = 20r_g$ (dashed) and $x_s = 30r_g$ (long-dashed). We see that with the increase in x_s, the

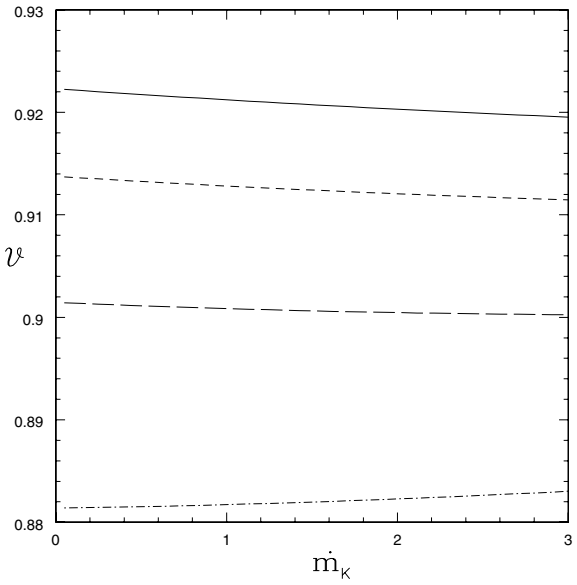

Figure 6. Variation of ϑ with $\dot{m}_K$, for $x_s = 20r_g$. The various curves correspond to $\ell = 0.3$ (solid), $\ell = 0.24$ (dashed), $\ell = 0.18$ (long-dashed) and $\ell = 0.12$ (dashed-dotted). The injection parameters are $z_{in} = 5r_g$, $v_{in} = 10^{-3}$.

acceleration is reduced. For $x_s = 10r_g$ (solid), we see that the jet is experiencing tremendous acceleration and within a short distance of $z \sim 40r_g$, it achieves a velocity ~ 0.9, and gradually settles to a terminal value of $\vartheta = 0.93$. As the shock location is increased to $x_s = 20r_g$ (dashed) and $x_s = 30r_g$ (long-dashed), acceleration is weaker and the terminal speeds achieved are $\vartheta = 0.9$ and $\vartheta = 0.88$ respectively. Thus, the terminal speed depends strongly on the shock location and decreases with increasing shock location.

In Fig. 7(b), we have plotted ϑ against ℓ. The solid curves correspond to $\dot{m}_K = 1.4$ and the dashed curves correspond to $\dot{m}_K = 2.4$. The shock locations, x_s, are marked on each pair of solid and dashed curves ($x_s = 10r_g, 20r_g, 30r_g$) in the figure. We see that in general ϑ increases with ℓ. We also see that, for particular values of x_s, $\dot{m}_K$ has very limited influence on ϑ (see each pair of solid and dashed curves marked with values of $x_s = 10, 20, 30$), and also that with increasing x_s, $\dot{m}_K$ is less and less effective in determining ϑ. In particular, the solid and the dashed curves marked $x_s = 10$ are distinguishable, but are increasingly less distinguishable for $x_s = 20$ and $x_s = 30$. With the increase in x_s, the inner edge of the Keplerian disc is increased. We also know that the magnitude of the Keplerian disc intensity is higher, closer to the black hole, i.e. if x_s increases then the size of the Keplerian disc and the Keplerian luminosity decreases. Thus with the increase of x_s, Keplerian radiation will be less effective in determining ϑ. Similar to Fig. 5(b), we also notice that if $\ell > 0.11$ for the pair of curves (solid and dashed) marked 10 (i.e. $x_s = 10$), then ϑ increases with decreasing $\dot{m}_K$, but decreases with decreasing $\dot{m}_K$, for $\ell < 0.11$. Though this cross-over value of ℓ increases with increasing x_s, i.e. for $x_s = 20r_g$, the cross-over occurs at $\ell = 0.15$, and for $x_s = 30r_g$ this occurs at $\ell = 0.24$. We also see that, generally, ϑ decreases with increasing x_s. In Fig. 7(c), ϑ is plotted against x_s, for $\dot{m}_K = 0.5$. The various curves correspond to $\ell = 0.24$ (solid), $\ell = 0.18$ (dashed), $\ell = 0.12$ (long-dashed) and $\ell = 0.06$ (dashed-dotted). It is clear that ϑ decreases with x_s, though for a fixed value of x_s, ϑ increases with ℓ. In Fig. 7(d), ϑ is plotted with x_s, for constant values of $\ell = 0.18$. Different curves correspond to $\dot{m}_K = 1.5$ (solid), $\dot{m}_K = 3$ (dashed) and $\dot{m}_K = 4.5$ (long-dashed). The first thing to notice is the weak dependence of ϑ on $\dot{m}_K$. We also notice that, for $x_s < 22r_g$, ϑ decreases with increasing $\dot{m}_K$ and for $x_s > 22r_g$, ϑ increases with increasing $\dot{m}_K$. The reason for this is that the CENBOL intensity falls with increasing x_s. Thus for larger x_s the radiative moments due to the CENBOL at infinite distances are comparable to those due to the Keplerian disc. Hence with increasing $\dot{m}_K$, ϑ increases, for exactly the same reason as has been presented while discussing Fig. 5(b). In general, one can conclude from Figs 7(a)–(d) that jets can be accelerated to up and around 90 per cent of the velocity of light, provided that $x_s \rightarrow 10r_g$–$20r_g$, and $\ell \rightarrow 0.1$–0.2. As we discussed earlier, such values of ℓ are not unreasonable when amplification of photon energy takes place due to Comptonization and $\tau \sim 1$. For smaller τ, the amplification factor is higher (so that $\ell \sim 1$ is achievable) but in that case, both the number of very energetic photons goes down and also the efficiency of depositing radiative momentum goes down dramatically.

In the preceding paragraphs of this subsection, we have studied the issue of radiative acceleration of jets, and its dependence on three parameters, namely x_s, ℓ and $\dot{m}_K$. In the case of CENBOL radiation, the information we have provided is through its total luminosity, but Keplerian luminosity is governed by two parameters x_s and $\dot{m}_K$ (see equation 11). To gain a better understanding, we now study how the relative proportions of CENBOL and Keplerian luminosity affect the terminal speed of the jet.

In Fig. 8(a), ϑ is plotted against ℓ_K/ℓ, the ratio of the Keplerian and CENBOL luminosities, for $x_s = 20r_g$. The various curves correspond to $\ell = 0.3$ (solid), $\ell = 0.24$ (dashed), $\ell = 0.18$ (long-dashed) and $\ell = 0.12$ (dashed-dotted). The ratio of luminosities is kept less than one to mimic the hard state of the accretion disc. We see that for $\ell = 0.12$, ϑ increases with the increase of Keplerian luminosity. For higher CENBOL luminosities (see the solid, dashed and long-dashed curves) we observe that ϑ decreases with increasing Keplerian luminosity. This has been addressed while discussing Figs 5(b), 6 and 7(b), i.e. for $x_s = 20r_g$, if $\ell < 0.15$, ϑ increases with the increase of Keplerian luminosity. It is thus clear that if $x_s = 20r_g$ then for ℓ higher than 0.15, jets can be accelerated to very high terminal velocities. In order to study the dependence of shock location and the Keplerian luminosity, in Fig. 8(b) we have plotted ϑ against ℓ_K/ℓ for $\ell = 0.24$. The Keplerian luminosity is thus increased from 3 per cent to 75 per cent of the CENBOL luminosity. The various curves correspond to $x_s = 10r_g$ (solid), $x_s = 20r_g$ (dashed) and $x_s = 30r_g$ (long-dashed). For $x_s = 10r_g$, ϑ is around 0.93 but decreases with the increase of Keplerian luminosity. With the increase in shock location the terminal velocity is less ($\vartheta = 0.91$ for $x_s = 20r_g$), but at the same time, the decrement of the terminal velocity due to the increase of Keplerian luminosity is also smaller. For $x_s = 30r_g$, $\vartheta \sim 0.895$ is smaller, but the change due to the increase of Keplerian luminosity is even less and ϑ remains almost constant. Thus we conclude that if the shock location is between $10r_g$ and $20r_g$ then jets can be accelerated to terminal speeds above 90 per cent of the velocity of light, for disc luminosities around 20 per cent of the Eddington luminosity.

4 DISCUSSION AND CONCLUDING REMARKS

It is well known that high-energy photons can produce particle–antiparticle pairs close to the inner edge of a disc. If the photon energy is $h\,\nu \gtrsim 2mc^2$, where h is Planck's constant, ν is the photon frequency and m is the electron (or positron) mass, then an electron–positron pair may be created. If, on the other hand, an electron and positron collide they will annihilate each other to produce two gamma-ray photons, a process called pair annihilation. Clearly, to produce electron-positron jets the pair-production

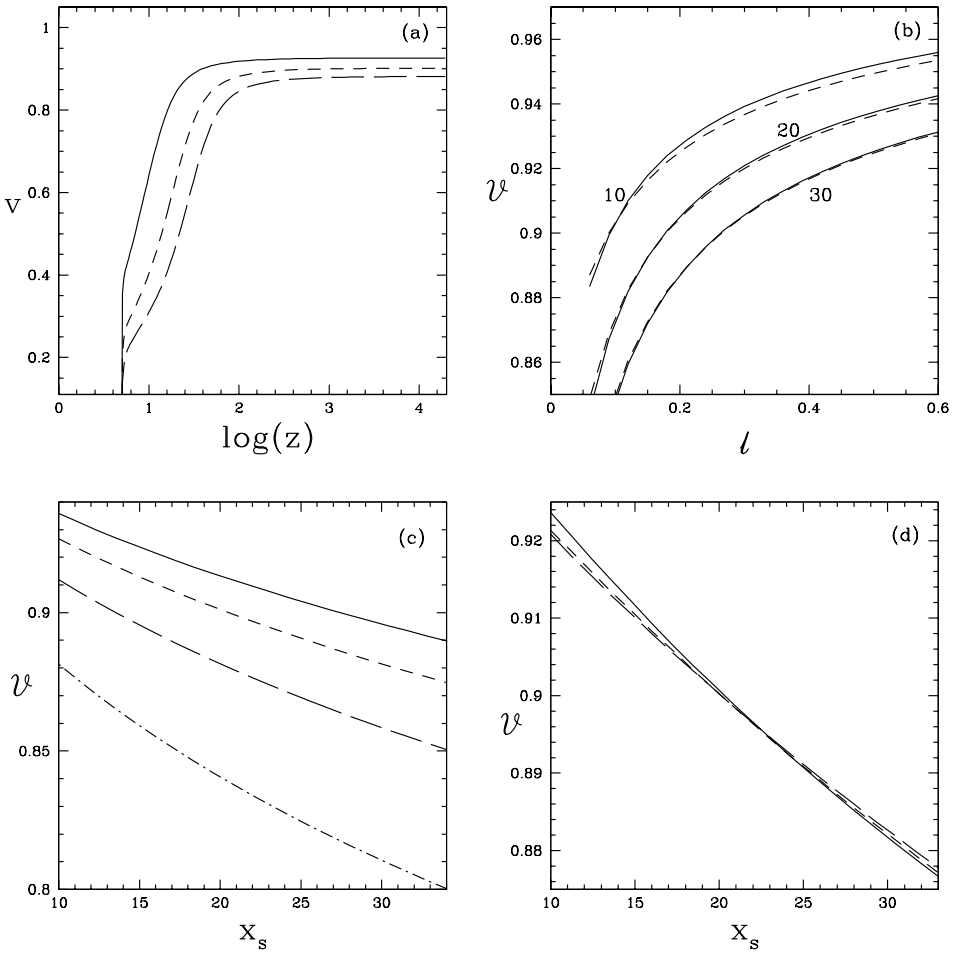

Figure 7. (a) Variation of v with $\log(z)$ for $\ell = 0.18$ and $\dot{m}_K = 0.5$. The various curves correspond to $x_s = 10r_g$ (solid), $x_s = 20r_g$ (dashed) and $x_s = 30r_g$ (long-dashed). (b) Variation of ϑ with ℓ. The solid curves correspond to $\dot{m}_K = 1.4$ and dashed curves correspond to $\dot{m}_K = 2.4$. The shock locations, x_s, are marked on each pair of solid and dashed curves ($x_s = 10r_g$, $20r_g$, $30r_g$). (c) Variation of ϑ with x_s, for $\dot{m}_K = 0.5$. The various curves represent $\ell = 0.24$ (solid), $\ell = 0.18$ (dashed), $\ell = 0.12$ (long dashed) and $\ell = 0.06$ (dash-dot). (d) Variation of ϑ with x_s, for $\ell = 0.18$. The various curves represent $\dot{m}_K = 1.5$ (solid), $\dot{m}_K = 3$ (dashed) and $\dot{m}_k = 4.5$ (long dashed). The injection parameters are $z_{in} = 5r_g$, $v_{in} = 10^{-3}$.

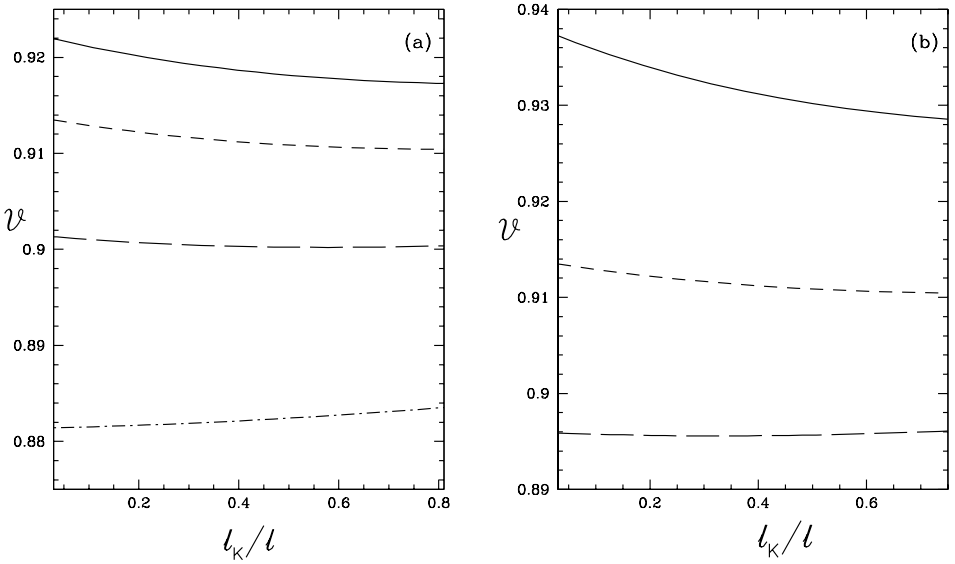

Figure 8. (a) Variation of ϑ with ℓ_K/ℓ for $x_s = 20$ for all the curves. The various curves correspond to $\ell = 0.3$ (solid), $\ell = 0.24$ (dashed), $\ell = 0.12$ (long-dashed) and $\ell = 0.12$ (dashed-dotted). (b) Variation of ϑ with ℓ_K/ℓ for $\ell = 0.24$. The various curves correspond to $x_s = 10r_g$ (solid), $x_s = 20r_g$ (dashed) and $x_s = 30r_g$ (long-dashed). The injection parameters are $z_{in} = 5r_g$, $v_{in} = 10^{-3}$.

process has to dominate over pair annihilation. Workers (e.g. Mishra & Melia 1993; Yamasaki et al. 1999) discussed the production of electron–positron pairs from the inner part of the accretion disc. Observationally, there are reports of pair-dominated jets (Sunyaev et al. 1992; Mirabel & Rodriguez 1998; Wardle et al. 1998) from galactic black-hole candidates to quasars. Though there is little doubt about the existence of pair-dominated jets, radiative acceleration of such jets, on the other hand, is a different issue altogether. If the number density of pairs created around the black hole is too high, then radiative acceleration would be ineffective. In this paper, we have ignored the details of formation of the pair plasma jets and have only concentrated on the radiative acceleration of optically thin pair-dominated jets.

In this paper, we supplied the CENBOL intensity, $I_{\rm C}$, and the shock location, $x_{\rm s}$, as free, but reasonable parameters. We have separately treated two velocity variables: (i) the equilibrium velocity $v_{\rm eq}$ and (ii) the actual velocity v. While $v_{\rm eq}$ decides how much velocity is allowed before deceleration sets in, v gives us what 'net' value of velocity is achieved by actual acceleration. We have shown that if only CENBOL radiation dominates over the radiation from the Keplerian disc, $v_{\rm eq} \sim 1$ is achieved within a few tens of Schwarzschild radii, but the same condition is achieved at over a thousand Schwarzschild radii for much higher values of Keplerian luminosity. From Figs 4(a) and (b), we have seen that as the Keplerian accretion rate is increased, $v_{\rm eq}$ decreases in the range $z \rightarrow 15r_{\rm g}$–$1500r_{\rm g}$.

From Fig. 3(d), we have seen that $(\tilde{E}_K + \tilde{P}_K) > 2\tilde{F}_K$ in this very range, so in this range the radiation drag is higher due to Keplerian radiation. This means that for higher values of ℓ and for fixed $x_{\rm s}$, i.e. for higher CENBOL intensity, the flow will tend to achieve very high velocities within a few tens of Schwarzschild radii, but at the same time if the Keplerian luminosity or ℓ_K is increased, then within the range $15r_{\rm g}$–$1500r_{\rm g}$, Keplerian radiation will tend to reduce the high velocities because of increased radiation drag.

From this study we generally conclude that:

(i) Radiative acceleration of electron–positron jets does achieve relativistic terminal speed.

(ii) The space-dependent part of the radiative moments from the post-shock region dominates the corresponding moments from the Keplerian disc.

(iii) In general, the terminal speed of jets increases with increasing post-shock luminosity.

(iv) The post-shock radiative intensity decreases with increasing shock location, so the terminal speed also decreases with increasing shock location.

(v) Keplerian radiation has a marginal effect in determining the terminal speed.

(vi) Our calculations show that, if the shock in accretion is located at around 10–20 Schwarzschild radii, and if the post-shock luminosity is about 10–20 per cent of the Eddington luminosity, then electron–positron jets can be accelerated to terminal speeds above 90 per cent of the speed of light.

ACKNOWLEDGMENTS

This work is supported in part by a grant from the ESA Prodex project; ESA Contract no. 14815/00/NL/SFe(IC) [IC] and Department of Science and Technology [SKC and SD], Government of India, through a grant no SP/S2/K-15/2001.

REFERENCES

Abramowicz M. A., Piran T., 1980, ApJ, 241, L7
Bridle A. H., Perley R. A., 1984, ARA&A, 22, 319
Biretta J. A., 1993, in Burgerella D., Livio M., Oea C., eds, Space Telesc. Sci. Symp. Ser., Vol. 6, Astrophysical Jets. Cambridge Univ. Press, Cambridge, p. 263
Chakrabarti S. K., 1989, ApJ, 347, 365 (C89)
Chakrabarti S. K., 1990, MNRAS, 243, 610 (C90)
Chakrabarti S. K., 1996, ApJ, 464, 664 (C96)
Chakrabarti S. K., 1997, ApJ, 484, 313 (C97)
Chakrabarti S. K., 1998, in Chakrabarti S. K., ed., Proc. Observational Evidence For Black Holes In The Universe. Kluwer, Dordrecht, p. 19
Chakrabarti S. K., 1999, A&A, 351, 185
Chakrabarti S. K., Mandal S., 2003, in Durouchoux P., Fuchs Y., Rodriguez J., eds, New Views on Microquasars, 117. CSP, Kolkata
Chakrabarti S. K., Titarchuk L., 1995, ApJ, 455, 623 (CT95)
Chakrabarti S. K., Titarchuk L., Kazanus L., Ebisawa K., 1996, A&AS, 120, 163 (CTKE96)
Chattopadhyay I., Chakrabarti S. K., 2000, Int. J. Mod. Phys. D, 9(1), 57
Chattopadhyay I., Chakrabarti S. K., 2002a, MNRAS, 333, 454
Chattopadhyay I., Chakrabarti S. K., 2002b, in Durouchoux P., Fuchs Y., Rodriguez J., eds, Proc. 4th Microquasar Workshop, CSP, Kolkata, p. 118
Chattopadhyay I., Das S., Mandal S., Chakrabarti S. K., 2003, in Chakrabarti S. K., Das S., Basu B., Khan M., eds, Proc. Recent Trends in Astro and Plasma Physics in India. CSP, Kolkata, p. 76
Das T. K., Chakrabarti S. K., 1999, Class. Quant. Grav., 16, 3879
Das S., Chattopadhyay I., Nandi A., Chakrabarti S. K., 2001, A&A, 379, 683
Ebisawa K., Titarchuk L., Chakrabarti S. K., 1996, PASJ, 48, 59
Fukue J., 1987, PASJ, 39, 309
Fukue J., 1996, PASJ, 48, 631
Fukue J., 2003, PASJ, 55, 451
Fukue J., Tojyo M., Hirai Y., 2001, PASJ, 53 555
Gallo E., Fender R. P., Pooley G. G., 2003, MNRAS, 344, 60
Icke V., 1980, AJ, 85, 329
Icke V., 1989, A&A, 216, 294
Junor W., Biretta J. A., Livio M., 1999, Nat, 401, 891
Kato S., Fukue J., Mineshige S., 1998, Black-hole Accretion Disks. Kyoto Univ. Press, Kyoto (K98)
Liang E. P. T., Thompson K. A., 1980, ApJ, 240, 271L
Lynden-Bell D., 1978, Phys. Scr., 17, 185
Mihalas D., Mihalas B. W., 1984, Foundations of Radiation Hydrodynamics. Oxford Univ. Press, Oxford (MM84)
Mirabel I. F., Rodriguez L. F., 1994, Nat, 371, 46
Mirabel I. F., Rodriguez L. F., 1998, Nat, 392, 673
Mishra R., Melia F., 1993, ApJ, 419, L25
Novikov I. D., Thorne K. S., 1973, in Dewitt C., Dewitt B., eds, Black Holes. Gordon and Breach, New York, p. 343 (NT73)
Paczynski B., Wiita P., 1980, A&A, 88, 23
Piran T., 1982, ApJ, 257, L23
Shakura N. I., Sunyaev R. A., 1973, A&A, 24, 337
Sikora M., Wilson D. B., 1981, MNRAS, 197, 529
Smith D. M., Heindl W. A., Markwardt C. B., Swank J. H., 2001, ApJ, 554, L41
Smith D. M., Heindl W. A., Swank J. H., 2002, ApJ, 569, 362
Sol H., Pelletier G., Assêo E., 1989, MNRAS, 237, 411
Sunyaev R., Churazov E., Gilfanov M., Dyachkov A., Khavenson N., Grebenev S., Kremnev R., Sukhanov K., 1992, ApJ, 389, L75
Yamasaki T., Takahara F., Kusunose M., 1999, ApJ, 523, L21
Wardle J. F. C., Homan D. C., Ojha R., Roberts D. H., 1998, Nat, 395, 457
Zensus J. A., Cohen M. H., Unwin S. C., 1995, ApJ, 443, 35

This paper has been typeset from a TEX/LATEX file prepared by the author.